Tailoring the mechanical potential of a PBF-LB/Med Al-Si-Cu alloy through heat treatment customization

Journal of Materials Research and Technology 44 (2026) 3371–3385

Contents lists available at ScienceDirect

Journal of Materials Research and Technology

journal homepage: www.elsevier.com/locate/jmrt

Tailoring the mechanical potential of a PBF-LB/Med Al-Si-Cu alloy through heat treatment customization

M.J. Yadegari, A. Martucci *, P. Fino, M. Lombardi

Department of Applied Science and Technology, Politecnico di Torino, Corso Duca Degli Abruzzi 24, 10129, Turin, Italy

ARTICLE INFO

Keywords:
Additive manufacturing
PBF-LB/M
Aluminum
AlSi10Cu8Mg
Heat treatment
T5
Direct aging

ABSTRACT

Al-Si and Al-Cu alloys are widely employed in laser-based powder bed fusion of metals (PBF-LB/M) and are well known for the fine cellular microstructures and high solute supersaturation achieved through rapid solidification, which contribute to their outstanding properties. However, most post-processing studies have focused on AlSi10Mg or Al–Si–Cu alloys containing Cu levels within the solubility limit of the Al matrix, while the direct-aging behavior of high-Cu compositions, such as AlSi10Cu8Mg, remains largely unexplored. In particular, the interaction between precipitation-related strengthening and the stability of the Al–Si–Cu-rich cellular network has not been systematically clarified. In this study, gas-atomized AlSi10Cu8Mg was processed by PBF-LB/M and directly aged from the as-built condition. The research was conducted in four successive stages. First, gas-atomized AlSi10Cu8Mg powders were processed by PBF-LB/M and the bulk samples were characterized in the as-built condition. Second, differential scanning calorimetry was used to identify the main transformation ranges and guide the selection of the aging temperatures. Third, the specimens were directly aged at 140–180 °C to promote controlled precipitation while preserving the cellular network, or at 250–350 °C to accelerate microstructural coarsening and network fragmentation. Finally, the phase constitution, microstructure, near-surface residual stress, hardness, and tensile response at room temperature and 200 °C were evaluated and correlated with the applied thermal conditions. The as-built alloy exhibited high strength but limited ductility. Aging at 160 °C promoted a moderate hardening response, with peak hardness after 10 h. The heat treatment at 160 °C for 24 h effectively preserved the as-built yield strength while reducing elongation by about 18 %. In contrast, the heat treatment at 250 °C for 4 h markedly improved ductility, increasing room-temperature elongation by approximately 50 %, although with a little reduction in yield strength. This treatment also enhanced the high-temperature tensile response, with elongation reaching 2.60 % at 200 °C, and reduced the near-surface residual stress by approximately 50 % compared with the as-built condition. These results demonstrate that the strength–ductility balance is governed by the interplay between precipitation-related processes and the preservation or fragmentation of the cellular network.

1. Introduction

The advent of metal additive manufacturing, particularly laser-based powder bed fusion of metals (PBF-LB/M), has opened new opportunities for aluminum alloys. PBF-LB/M enables the fabrication of complex, near-net-shape components with minimal material waste, while rapid solidification promotes the formation of fine microstructures with potentially superior mechanical properties [1,2]. As a result, aluminum alloys produced by PBF-LB/M have become highly attractive for lightweight structures in transportation, aerospace, and defense sectors [2,3].

Despite the rapid growth of PBF-LB/M technologies, the portfolio of high-strength aluminum alloys that can be processed reliably remains remarkably narrow. In particular, 2xxx- and 7xxx-series alloys, although renowned for their strong precipitation-hardening potential, exhibit a pronounced susceptibility to hot cracking during additive manufacturing due to their wide solidification intervals [4–6].

Studies have shown that adding silicon significantly improves melt fluidity, and when introduced in amounts close to the eutectic composition, it effectively narrows the solidification interval, thereby mitigating hot-cracking tendencies. Within this framework, incorporating ~10 wt% Si promotes the formation of a fine eutectic Si network capable

* Corresponding author.
E-mail address: alessandra.martucci@polito.it (A. Martucci).

https://doi.org/10.1016/j.jmrt.2026.08.105
Received 3 July 2026; Received in revised form 11 August 2026; Accepted 12 August 2026
Available online 13 August 2026

of accommodating thermally induced strains during rapid solidification [7,8]. However, their mechanical performance often falls short of industry requirements, motivating ongoing efforts to use the near-eutectic Al–Si system as a processable baseline and explore the addition of tailored alloying elements [9]. In this context, the addition of Cu to Al–Si alloys has attracted significant interest in particular in the aerospace industry, where the Cu-containing Al alloys account for approximately 45 % of the total aluminum alloy portfolio used in civil aircraft [10].

However, the processing of Cu-containing Al alloys requires careful control, as their processability in PBF-LB/M has begun to be investigated using compositions conventionally employed in traditional processing routes [11,12]. For instance, a study on PBF-LB/M 2024 Al has reported severe hot cracking influenced by scanning speed, eutectic phase formation, and residual stress development [13], while similar behavior has been observed in high-strength Al–Cu–Mg–Mn alloys where cracking was closely linked to single-track spreading, thermal conditions, and processing parameters [14].

Studies already published in the literature employed the addition of Cu on Al-Si systems, aiming to exploit the excellent processability of near-eutectic Al–Si systems while enhancing mechanical performance through Cu solid solution strengthening and the precipitation of reinforcing phases, successfully producing a refined cellular α-Al microstructure and a supersaturated matrix, which resulted in increased hardness and yield strength. For example, PBF-LB/M Al–Si–Cu–Ni alloys have been reported to develop a cellular heterostructure enriched in Si and Cu-containing phases, which contributes to strengthening but may also limit ductility if brittle networks remain continuous. These observations support the need to understand not only precipitation hardening, but also the stability and fragmentation of the cellular network during post-processing [15–17].

Additional studies explored the mechanical blending of Cu powder into the well-established AlSi10Mg system; however, this approach inevitably led to local compositional inhomogeneities and pronounced microstructural variability after PBF-LB/M processing [18–21]. Nevertheless, it highlighted the potential of Cu additions by demonstrating enhanced mechanical performance compared to the base AlSi10Mg alloy, thereby motivating further research toward more compositionally controlled alloy design strategies. To mitigate the inhomogeneities coming from the mechanical blending, research efforts shifted toward gas-atomized pre-alloyed powders, such as AlSi10Cu4Mg. Pre-alloying ensures chemical uniformity at the particle scale and stabilizes the solidification pathway during PBF-LB/M, enabling more reliable control over the balance between solid-solution supersaturation and boundary-related strengthening mechanisms [22,23].

Exploiting the enhanced solid solubility enabled by the rapid solidification inherent to PBF-LB/M, previous studies have extended Cu additions to compositions that remain only partially explored to date. In particular, the AlSi10Cu8Mg composition has been shown to develop microstructures closely resembling the well-established AlSi10Cu4Mg system, remaining fully processable with appropriate parameter optimization and exhibiting 22 % higher hardness than its 4 wt% Cu counterparts. Moreover, the elevated Cu content enables higher levels of supersaturation, making the AlSi10Cu8Mg alloy especially well-suited for precipitation strengthening during subsequent aging treatments [24].

Alongside alloy design, heat treatment plays a crucial role in controlling the properties of PBF-LB/M-processed aluminum alloys. In conventional precipitation-hardenable aluminum alloys, a T6 treatment consists of solution heat treatment, rapid quenching, and artificial aging. During solution treatment, the alloy is held at an elevated temperature to dissolve soluble secondary phases and redistribute alloying elements within the α-Al matrix. Rapid quenching subsequently suppresses equilibrium precipitation and retains the dissolved elements in a metastable supersaturated solid solution. Artificial aging then promotes the controlled formation of fine precipitates that impede dislocation motion and increase strength and hardness. The resulting mechanical response depends on precipitate size, coherency, distribution, and interparticle spacing, as well as on the evolution of the surrounding microstructure [25–27]. In Cu-containing Al-based alloys, elevated solution-treatment temperatures may additionally promote local incipient melting of low-melting Cu-rich constituents [25–30].

The initial condition of PBF-LB/M alloys differs substantially from that of conventionally cast or wrought materials. During PBF-LB/M, each melt pool undergoes rapid solidification and cooling, thereby retaining Si, Cu, and other alloying elements within the α-Al matrix at concentrations above their equilibrium solubility. This process-induced supersaturation is sometimes described as a self-quenching-like effect and provides the driving force for subsequent direct aging [21,23,31,32]. However, it should not be regarded as a conventional solution-treatment and quenching cycle. No controlled bulk isothermal hold is applied to dissolve secondary phases and homogenize the entire component. Previous studies demonstrate that the direct-aging response of PBF-LB/M Al–Si alloys is strongly dependent on alloy composition and the initial non-equilibrium microstructure.

Maeshima et al. investigated the nanoscale evolution of directly aged PBF-LB/M AlSi10Mg using scanning transmission electron microscopy and atom-probe tomography [31]. During the initial aging stage, a high number density of solute clusters formed within the α-Al cells, while prolonged aging promoted the precipitation of fine Si particles with diameters of approximately 50 nm. Both clustering and Si precipitation contributed to the age-hardening response. Megahed et al. [30] demonstrated that extreme over-aging of PBF-ed AlSi10Mg produces coarse Si and Mg_2Si precipitates (~2 μm), greatly reducing strength but increasing ductility from approximately 2 to 20 %. More recently, Batalha et al. systematically evaluated direct aging of PBF-LB/M AlSi10Mg and showed that aging at 150 °C for 2 h preserved the eutectic Si network while promoting a dense population of nanometric Si particles [32]. This treatment increased the yield strength and ultimate tensile strength by 17 and 13 %, respectively, without prior solution treatment. In contrast, higher-temperature treatments disrupted the cellular structure and coarsened the Si particles, resulting in reduced strength. Sathishkumar et al. compared cast and PBF-LB/M-processed AlSi10Mg after direct aging and reported that the strength improvement in the additively manufactured alloy resulted from the combined effects of precipitation and cellular-boundary strengthening [33]. Kramer et al. similarly observed that increasing thermal exposure progressively fragmented the Si-rich cellular network and promoted the agglomeration and coarsening of Si particles, with a corresponding reduction in hardness [34]. This behavior reflects the fundamental trade-off in precipitation-hardened systems: under-aged conditions maximize strength by forming finely dispersed precipitates that impede dislocation motion, whereas over-aging promotes ductility as precipitates coarsen and residual stresses relax.

The introduction of Cu adds further complexity to this response. Bosio et al. investigated an in-situ-alloyed AlSi10Mg–4Cu system and reported that direct aging at 175 °C for 1 h produced the maximum hardness response via θ'/θ-Al_2Cu precipitation while maintaining the fine Si network [21]. However, the mechanically blended feedstock also produced local Cu inhomogeneity and limited ductility. Martin et al. studied a pre-alloyed AlSi10Cu4Mg powder and reported hardness values of approximately 175 HV after aging at 180 °C for 4 h and 183 HV after aging at 160 °C for 16 h [23].

Despite the progress achieved in the development of PBF-LB/M-processed Al–Si–Cu–Mg alloys, the post-processing response of high-Cu compositions remains insufficiently understood. This represents an important knowledge gap, because the higher Cu content in AlSi10Cu8Mg is expected to increase the degree of supersaturation generated during rapid solidification and, consequently, to enhance the potential for precipitation-related strengthening during subsequent aging. At the same time, excessive precipitation, coarsening, residual stress retention, or degradation of the PBF-LB/M cellular network may reduce ductility and damage tolerance. Therefore, an effective heat-treatment strategy

must balance strengthening, stress relaxation, and microstructural stability.

The overall aim of this work was to determine how single-step direct aging controls the microstructure and mechanical response of pre-alloyed AlSi10Cu8Mg fabricated by PBF-LB/M without a separate conventional solution-treatment and quenching step. First, the as-built reference condition was established by characterizing its phase constitution, cellular solidification structure, hardness, near-surface residual stress, and tensile behavior. Second, DSC and hardness measurements were used to design and evaluate low-temperature, long-duration and high-temperature, short-duration direct-aging strategies and to identify representative peak-aged and overaged conditions. Third, the effects of the selected heat treatment conditions on the XRD-detectable phase constitution, α-Al lattice parameter, cellular-network morphology, grain-boundary structure, and near-surface residual stress were examined. Finally, the resulting thermal and microstructural changes were correlated with tensile behavior at room temperature and 200 °C to identify the treatment providing the most favorable strength–ductility balance among the investigated conditions.

2. Materials and methods

2.1. Material and PBF-LB/M process parameters

The AlSi10Cu8Mg powder was produced in-house using a PSI HERMIGA 100/10 VI vacuum induction gas atomisation system, starting from AlSi10Mg and pure Cu ingots. Prior to vacuum induction melting, a backfilling procedure was performed to limit the evaporation of volatile alloying elements. Owing to the pronounced oxidation susceptibility of Al-based alloys, gas atomisation was carried out under a high-purity argon atmosphere. The atomisation parameters were selected according to the operating conditions recommended by PSI Ltd., the equipment manufacturer. Given the high reactivity of the resulting powder, a passivation treatment was subsequently applied to reduce the risk of ignition and explosion. Before characterisation, the powder was sieved to obtain a particle size fraction ranging from 20 to 63 μm, suitable for PBF-LB/M processing. The chemical composition of AlSi10Cu8Mg is reported in Table 1. The chemical composition of the investigated alloy samples was determined by inductively coupled plasma optical emission spectroscopy. The analysis was performed by TEC Eurolab using an iCAP 7200 plasma spectrometer according to the laboratory internal method MI 056 Rev. 15 (2022). Elemental concentrations were reported in weight percent, with the base element calculated as the balance.

The particle size distribution was measured using a Mastersizer3000 laser diffraction particle size analyser and revealed D10, D50 and D90 values of 17.3, 28.8 and 45.6 μm, respectively. The powder apparent density (ρa) and tap density (ρt) were measured three times according to ASTM B417-18 [35] and ASTM B527-15 [36], respectively. The Hausner ratio (H) was then calculated as the ratio of the tap and apparent densities as $H = \rho t/\rho a$. Lower H values indicate better powder flowability and packing behavior, whereas higher values are associated with increased interparticle friction and poorer spreading. According to Sutton et al. [37], powders with $H < 1.25$ are generally considered suitable for PBF-LB/M processing. For the AlSi10Cu8Mg powder, an H value of 1.09 was measured, confirming its good flowability and suitability for successful PBF-LB/M processing.

PBF-LB/M production was performed using a Print Sharp 250 system equipped with a single-mode infrared fiber laser (500 W as maximum power). The system provides a build volume of 258 × 258 × 330 mm^3 and supports a build rate ranging from 12 to 30 cm^3/h. Samples were fabricated on an Al build platform preheated to 100 °C in order to reduce thermal gradients, mitigate residual stresses, and stabilize the melt pool. A stripe scanning strategy was implemented, with each successive layer rotated by 67° relative to the previous one. To identify suitable processing parameters for the AlSi10Cu8Mg alloy, a Design of Experiments (DoE) approach was carried out by varying laser power (P) and scan speed (v), while keeping hatch distance and layer thickness constant. Specifically, laser power was varied between 200 and 400 W, and scan speed between 200 and 1500 mm/s. The hatch distance was fixed at 0.14 mm, corresponding to the optimized value previously identified for a similar alloy system (AlSi10Mg) processed on the same machine. The layer thickness was set to 30 μm according to the machine supplier's recommendations for Al-based alloys, ensuring adequate overlap between tracks and promoting a uniform thermal distribution. For each parameter combination, the relative density of the fabricated samples was measured using the Archimedes method and image analysis through ImageJ software. The DOE results demonstrated that relative densities above 99.5 % were consistently achieved over a broad processing window. The optimal condition was identified at P = 250 W and v = 1250 mm/s, corresponding to a relative density of 99.9 % with negligible standard deviation. Under these conditions, the microstructure was free of defects, and only a minimal amount of fine, spherical gas porosity was observed, which is not expected to significantly affect the mechanical response.

Cubic specimens (10 × 10 × 10 mm^3) and flat tensile specimens printed in the horizontal orientation, were fabricated on an AlSi10Mg cast platform. Fig. 1 illustrates the geometry of the reduced-size flat dog-bone tensile specimen used in this study. The specimen had a total length of 135 mm (L), a gauge length of 35 mm (G), a gauge width of 5 mm (W), a grip-section width of 7 mm (C) and thickness of 4 mm.

Table 1
Chemical composition of AlSi10Cu8Mg.

Element (%)	Al	Si	Cu	Fe	Mg	Mn	Ti
AlSi10Cu8Mg	Balance	9.18	8.46	0.39	0.22	0.11	0.07

2.2. Heat treatment conditions

The precipitation behavior of the strengthening phases was examined using DSC with a Setaram TGA 92 16.18/DSC system. The analysis was performed over a temperature range of 20–450 °C following a three-stage thermal cycle. First, the samples were heated from room temperature to 450 °C at a constant rate of 10 °C/min. This was followed by a 5-min isothermal hold at 450 °C. Finally, the samples were cooled back to the initial temperature at 20 °C/min.

All aging treatments were applied directly to specimens in the as-built condition; no separate conventional solution-treatment or quenching step was performed before aging.

The aging temperatures were selected from the principal thermal events observed in the DSC thermogram of the as-built alloy. Low-temperature treatments at 140, 160, and 180 °C were selected below and around the onset of the first exothermic event to investigate controlled clustering and precipitation while limiting degradation of the as-built cellular network. High-temperature treatments at 250, 300, and 350 °C were selected at and above the first exothermic maximum and toward the second transformation region to investigate accelerated precipitation, overaging, particle coarsening, and cellular-network decomposition. The treatment durations were then evaluated through the corresponding hardness–time evolution and the residual exothermic response measured by DSC after aging.

The cubic specimens were heat treated in a Binder FD 23 furnace. Each specimen was introduced individually into the furnace, which had been preheated and thermally stabilized at the target temperature for at least 30 min prior to loading. Temperature fluctuations during insertion were carefully controlled, and the furnace temperature did not deviate by more than 5 °C from the set point. Upon completion of each heat-treatment cycle, the specimens were removed from the furnace and allowed to cool naturally to room temperature in ambient air. Table 2 summarizes the complete heat-treatment schedule developed for the AlSi10Cu8Mg alloy clarifying the acronyms used.

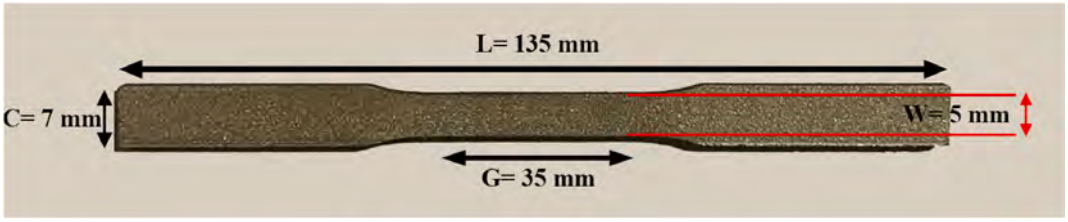

Fig. 1. Geometry and dimensions of the reduced-size flat dog-bone tensile specimen used in this study.

Table 2
Heat treatment procedure and acronyms for heat-treated AlSi10Cu8Mg samples.

Temperature (°C)	Times (h)	Acronym
140	8, 10, 12, 16, 20, 24, 32, 48	HT140-8| HT140-10| HT140-12| HT140-16| HT140-20| HT140-24| HT140-32| HT140-48
160	8, 10, 12, 16, 20, 24, 32, 48	HT160-8| HT160-10| HT160-12| HT160-16| HT160-20| HT160-24| HT160-32| HT160-48
180	3, 6, 12, 24	HT180-3| HT180-6| HT180-12| HT180-24
250	2, 4, 12	HT250-2| HT250-4| HT250-12
300	2, 4, 8	HT300-2| HT300-4| HT300-8
350	2, 4	HT350-2| HT350-4

2.3. Characterization methods

Microstructural characterization was performed on cubic specimens following heat treatment and in the as-built state. Sections were extracted parallel to the build direction, mounted in conductive resin, and subsequently ground and polished to a mirror finish using a colloidal silica suspension. To reveal melt pool boundaries, phase morphology, and grain structure, samples were etched in Keller's reagent for 10 s. Optical microscopy was conducted using a Leica DMI5000 M system, and micrographs were processed and analyzed with ImageJ software. High-resolution microstructural examination was further carried out using a JEOL JCM-7000 scanning electron microscope (SEM) operated under high vacuum. Secondary electron (SE) and backscattered electron (BSE) modes were employed to characterize surface morphology and contrast variations, while elemental distributions were assessed via energy-dispersive X-ray spectroscopy (EDS). EBSD analysis was performed on the as-built and selected heat-treated samples using a Tescan S9000G™ FIB-SEM operated at 20 kV and 10 nA, with a working distance of approximately 7 mm and a 70° sample tilt. EBSD maps were acquired with a step size of approximately 1.11 μm. EBSD analysis was also employed to evaluate the distribution of grain boundary misorientations, distinguishing between high-angle grain boundaries (HAGBs, >15°) and low-angle grain boundaries (LAGBs, <15°), with grains defined as regions enclosed by HAGBs.

Phase analysis was performed by X-ray diffraction (XRD) using a Malvern Panalytical Empyrean X-ray diffractometer in Bragg–Brentano configuration. Cu Kα radiation was used, generated at 40 kV and 40 mA, with a wavelength of $\lambda = 0.154$ nm. The XRD pattern of the as-built sample was collected over a 2θ range of 20–140°, while the heat-treated samples were scanned over a 2θ range of 15–140°. The step size was 0.003°, with a counting time of 180 s per step. A 1/4°–1/2° slit configuration was used. During acquisition, the samples were rotated with a revolution time of 8 s to improve measurement statistics and reduce orientation effects. Phase identification was performed by comparison with reference diffraction patterns for α-Al, Si, and θ-Al_2Cu.

Near-surface residual stresses were measured on cubic specimens using X-ray diffraction with a Pulstec μ360X system operated at 30 kV with a manganese cathode. For each condition, measurements were performed at five spatially separated positions on a surface parallel to the build direction. The mean value and standard deviation of the five measurements were calculated to evaluate the spatial variation of the measured near-surface stress. The approximate X-ray penetration depth was 30–50 μm. Therefore, these measurements characterize a local near-surface stress condition and do not represent the through-thickness or volume-averaged residual-stress field of the specimens. The results were used to compare the relative thermal-relaxation response of the investigated conditions.

Mechanical characterization included Vickers microhardness testing conducted according to ASTM E384 [38] using a VMHT microhardness tester. Indentations were made on polished cross-sections under a test load of 0.5 kgf and a dwell time of 10 s. A total of ten indentations were performed, and the average value was reported.

Monotonic tensile testing was carried out at room temperature and 200 °C using a Zwick-Roell BT1-FR100 universal testing machine equipped with an extensometer for strain measurement. The tests were performed following the general procedure of ASTM E8/E8M [39], while using a reduced-size flat dog-bone specimen geometry adapted to the dimensional constraints of PBF-LB/M fabrication. The specimen had a total length of 135 mm, a gauge length of 35 mm, a gauge width of 5 mm, with 4 mm thickness, and a grip-section width of 7 mm, as shown in Fig. 1. The crosshead displacement rate was 1 mm/min. For each heat-treatment condition and testing temperature, five tensile specimens were tested under nominally identical conditions. Yield strength, ultimate tensile strength and elongation were calculated for each specimen.

3. Experimental results and discussion

3.1. As-built microstructure

The microstructure of the alloy in the as-built condition was first examined to establish a reference state prior to heat treatment. Fig. 2 presents the as-built microstructure of the alloy before and after etching. In the unetched condition (Fig. 2a), the characteristic "fish-scale" morphology typical of PBF-LB/M processing is observed. The build direction (Z) is indicated, and the melt pool boundaries (MPBs) appear as shallow, overlapping arcs. Small, rounded pores are visible in the unetched section and are consistent with gas-related porosity. At this stage, individual grains cannot be resolved, and the contrast is dominated by melt pool topology. Similar morphologies were reported in other PBF-LB/Med materials [40,41].

After etching (Fig. 2b), the microstructure within each melt pool becomes significantly more distinct. The etchant preferentially reveals solidification features, highlighting elongated columnar grains that grow epitaxially along the direction of the maximum thermal gradient. These grains follow the curved melt pool contours, producing a textured structure in which grain boundaries align with MPBs. The columnar morphology reflects directional solidification governed by repeated thermal cycling during the layer-by-layer manufacturing process.

Quantitative analysis, performed using ImageJ, shows an average grain size of 17.05 μm, measured using the mean linear intercept method in accordance with ASTM E112 [42]. The melt pool dimensions exhibit an average depth of 118.75 ± 22.15 μm and a width of 154.17 ± 38.98 μm. The resulting width-to-depth ratio of approximately 1.3 is consistent with typical PBF-LB/M melt pool geometries reported for Al-Si-based alloys processed under moderate laser energy input. This ratio reflects a conduction-mode melt pool, in agreement with the

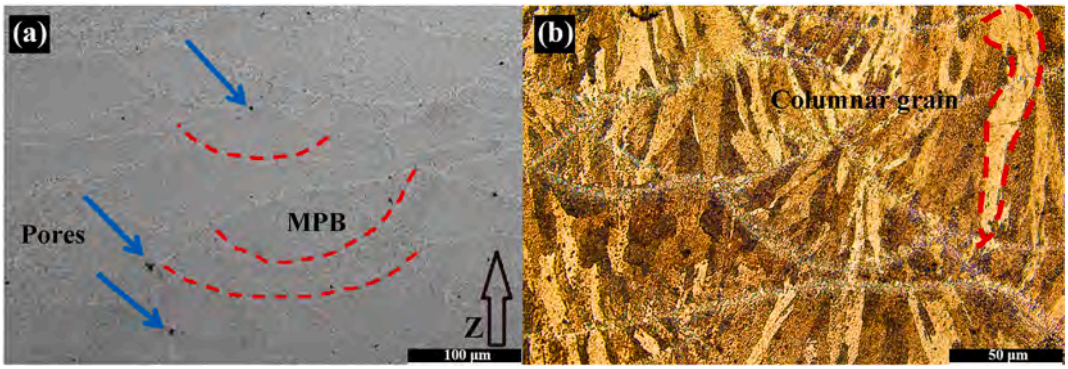

Fig. 2. Optical micrographs of the as-built PBF-LB/M AlSi10Cu8Mg alloy on a section parallel to the build direction: (a) unetched condition showing overlapping melt pools, melt-pool boundaries, and rounded pores; and (b) Keller-etched condition revealing the columnar solidification structure and melt-pool boundaries. The build direction, Z, is indicated.

absence of deep keyhole features in the microstructure [43].

To better resolve the solidification substructure of the as-built material, the etched surface was examined at higher magnifications using SEM (Fig. 3). As shown in Fig. 3a, the microstructure is composed of ultrafine cellular and cellular-dendritic features that align with the local thermal gradients defined by the melt pool geometry. Consistent with observations reported by Bosio et al. [21], distinct microstructural regions can be identified across the melt pool depending on cooling conditions and solute redistribution.

The region highlighted in red (Fig. 3b) corresponds to the melt pool core, where the solidification rate and cooling rate are highest. This zone exhibits a dense, fine cellular-dendritic network with a continuous eutectic skeleton decorating the cell boundaries. Such refinement reflects the extremely high cooling rate (product of thermal gradient G and solidification velocity R), which promotes narrow primary cells and thin interdendritic channels.

Approaching the melt pool boundary (blue region in Fig. 3c), the cellular morphology becomes progressively coarser. This transition is driven by a reduction in the local thermal gradient and an increase in constitutional undercooling near the curved melt pool interface. In Cu-containing Al alloys, this region also tends to accumulate solute, especially Cu and Si, which segregate into the interdendritic channels during solidification. The result is a cellular–dendritic structure with thicker eutectic films and more pronounced columnar elongation of α-Al cells. These features reflect reduced cooling rate, solute back-diffusion, and limited remelting–resolidification effects typical of the melt pool periphery [21,44,45].

In the SEM contrast, the α-Al matrix appears as the darker phase, while the bright interdendritic network seems to correspond to Si-rich eutectic regions and Cu-rich precipitate clusters. The EDS maps (Fig. 3d) confirm this interpretation. Si is enriched along the cell and dendrite boundaries, forming the continuous eutectic skeleton. Cu shows strong segregation in the same interdendritic channels, with the brightest signals concentrated along melt pool overlap regions.

This localized enrichment is consistent with repeated thermal cycling during successive laser scan tracks, which promotes microsegregation and solute accumulation at melt pool borders [46]. Furthermore, the refinement effect of Cu is well documented. Vanzetti et al. [44] demonstrated that increasing Cu content enhances the volume fraction of interdendritic phases and reduces secondary dendrite arm spacing relative to lower-Cu aluminum alloys, a trend also reported by Bobel et al. [47]. The present observations are in agreement with those findings, as the as-built microstructure shows closely spaced interdendritic networks enriched in Cu and Si.

3.2. Heat treatment optimization

Fig. 4 presents the DSC profile obtained for the as-built AlSi10Cu8Mg alloy. The DSC thermogram of the AlSi10Cu8Mg alloy reveals a distinct low-temperature exothermic event beginning at approximately 175 °C (onset) and reaching its maximum near 240 °C, which marks the precipitation from the supersaturated solid solution. Compared with the behavior of lower-Cu alloys reported in the literature [21], the AlSi10-Cu8Mg composition exhibits a substantially higher exothermic enthalpy and broader peak profiles. This indicates a larger precipitate volume fraction and a more intricate precipitation sequence [12].

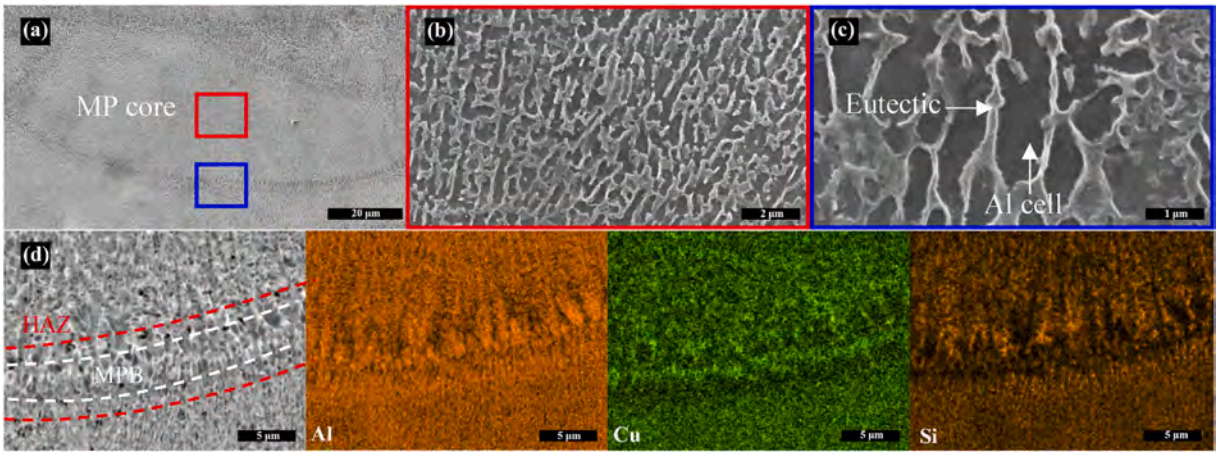

Fig. 3. SEM micrographs of the etched as-built microstructure (a) Overview of the melt pool revealing fine cellular–dendritic patterns (b) Fine cellular-dendritic structure in the melt pool core (c) Coarser cellular-dendritic morphology near the melt pool boundary (d) EDS elemental maps.

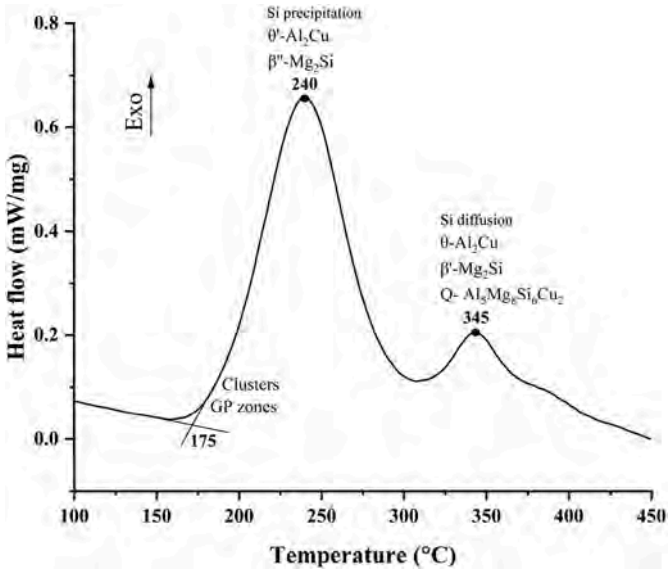

Fig. 4. DSC curve obtained from the as-built AlSi10Cu8Mg alloy sample.

The precipitation response of Al–Si–Cu–Mg alloys is complex because several solutes and strengthening reactions may evolve over overlapping temperature ranges. Based on previous studies of PBF-LB/M Al–Si–Mg and Al–Si–Cu–Mg alloys, the first exothermic event is interpreted as a combination of solute clustering, nanoscale Si precipitation, Mg–Si-related precipitation, and early-stage Cu-rich precipitation [27, 48–50]. The second exothermic event near 345 °C is consistent with the progression toward coarser and more thermally stable Si-, Mg–Si-, and Cu-containing constituents [21,44,51].

Silicon plays two distinct roles in the thermal response of the investigated alloy. The pre-alloyed powder contained 9.18 wt% Si. During rapid PBF-LB/M solidification, a portion of the Si is retained in the supersaturated α-Al matrix, while the remainder forms the Si-rich interdendritic cellular network. During low-temperature aging, retained Si may participate in solute clustering and the formation of nanoscale Si-rich precipitates, while the pre-existing cellular network remains largely continuous. Si may also interact with Mg in Mg–Si-related precipitation and, in the presence of Cu, contribute to more complex Cu–Mg–Si-containing precipitates.

As described in Section 2.2, the heat treatment procedures were designed based on the as-built DSC results. Low-temperature aging was conducted at 140, 160, and 180 °C (within the early stage of the exothermic peak), while high-temperature aging was performed at 250, 300, and 350 °C (above the peak region). After the heat treatments, the specimens were characterized using Vickers hardness and DSC results. For a consistent comparison, all DSC datasets were normalized and aligned to a common baseline reference.

Fig. 5 illustrates the Vickers hardness evolution and the corresponding DSC results obtained during low-temperature aging. In the low-temperature regime, the alloy demonstrates a classic age-hardening profile (Fig. 5a). AlSi10Cu8Mg in the as-built condition exhibited a hardness of 173 HV0.5, and a peak hardness of 191 HV0.5 was achieved after HT160-10. This trend is consistent with the DSC response at 160 °C (Fig. 5c), where the substantial reduction of the first exothermic event indicates that precipitation-related reactions had progressed during aging. The hardness increase is attributed to the combined effects of solute clustering and the formation or redistribution of fine

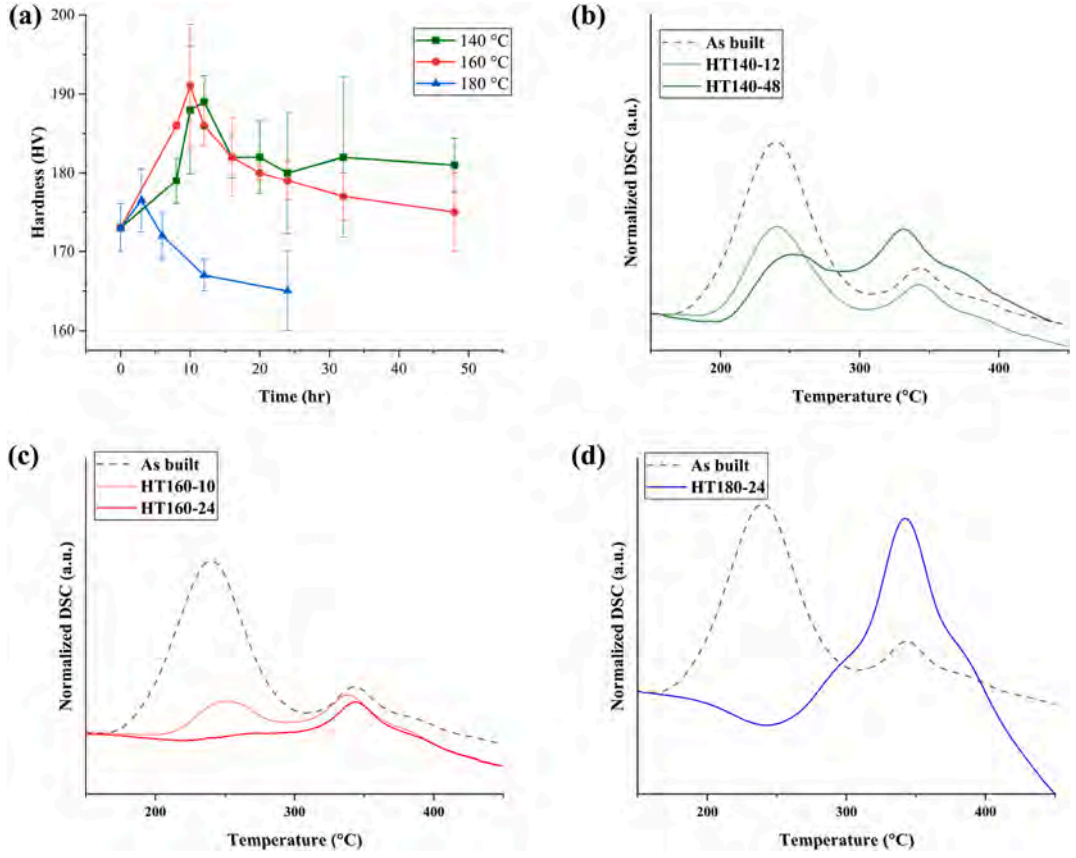

Figure 5. (a) Evolution of Vickers microhardness in the AlSi10Cu8Mg alloy during the low-temperature aging regime (140–180 °C), and (b–d) normalized DSC curves comparing the as-built condition with selected aging treatments at (b) 140 °C, (c) 160 °C, and (d) 180 °C. Hardness values represent the mean ± standard deviation of ten indentations per condition.

strengthening features within the α-Al matrix. Although aging at 140 °C ultimately yields a comparable hardness (~190 HV0.5 after 12 h), the kinetics are markedly slower. This sluggish response reflects the nucleation-limited behavior captured in the DSC thermograms (Fig. 5b), where up to 48 h was required to fully establish the precipitate population. The peak hardness obtained in the present AlSi10Cu8Mg alloy is higher than values previously reported for lower-Cu PBF-LB/M systems. Martin et al. [23] reported approximately 183 HV for pre-alloyed AlSi10Cu4Mg after direct aging at 160 °C for 16 h, compared with 191 HV0.5 after 10 h at the same temperature in the present study. Bosio et al. obtained the peak-aging response of an in-situ-alloyed AlSi10Mg–4Cu material after only 1 h at 175 °C [21].

To provide deeper insight, the aging response at 140 °C illustrates the transition from solute cluster formation to the onset of critical nucleation (Fig. 5b). After 12 h (HT140-12), the first exothermic peak (~240 °C) decreases in magnitude relative to the as-built condition, indicating partial consumption of the supersaturated solute to form early-stage clusters (GP zones). The most notable effect appears after 48 h (HT140-48): the second exothermic peak (~330–345 °C) becomes significantly taller and shifts to a lower onset temperature. This behavior reflects nucleation-assisted kinetics [52]. Prolonged holding at 140 °C generates a dense population of chemically enriched, thermodynamically stable nuclei. During DSC heating, these pre-existing nuclei bypass the nucleation energy barrier, allowing the transformation to proceed predominantly as a growth-controlled process. The synchronized growth of these nuclei produces a sharper, more intense exothermic peak than the broader nucleation-limited peak observed in the as-built material. This behavior can also suggests limited Mg_2Si precipitation at 140 °C, in agreement with previous studies reporting that Mg_2Si formation requires either higher aging temperatures or substantially longer exposure times [23].

At 160 °C (Fig. 5c), the DSC curves demonstrate a gradual reduction in the driving force for precipitation. After 10 h, HT160-10 retains a small residual first exothermic event, suggesting that the precipitation-related reactions associated with this temperature range were not fully completed during aging. By 24 h (HT160-24), this first peak disappears entirely, yielding a flat baseline up to 300 °C. This indicates that the precipitation-related reactions associated with the first exothermic event had progressed substantially during HT160-24, leaving a smaller remaining thermal response during the subsequent DSC scan. The lower height of the second peak compared with the as-built sample further indicates that the alloy is energetically closer to equilibrium, leaving less stored chemical energy for release during high-temperature transformation.

The HT180-24 condition (Fig. 5d) shows that the material has surpassed the peak-hardening stage associated with the first precipitation sequence. The absence of the first peak confirms that precipitation of metastable phases is fully completed. The second peak remains present but exhibits a shift consistent with altered transformation kinetics. This DSC response aligns with the hardness data (Fig. 5a), where samples aged at 180 °C show reduced hardness compared with those aged at 160 °C (178 HV0.5 for HT160-24 vs. 165 HV0.5 for HT180-24). The higher aging temperature promotes coarsening of previously formed fine precipitates, reducing coherency strains and thus lowering hardness, while simultaneously promoting nucleation of more stable phases as reflected by the prominent second peak.

Fig. 6 illustrates the Vickers hardness evolution and the corresponding DSC results obtained during high-temperature aging. The high-temperature regime (Fig. 6a) is dominated by rapid and pronounced softening. At 250 °C, near the DSC-identified peak precipitation

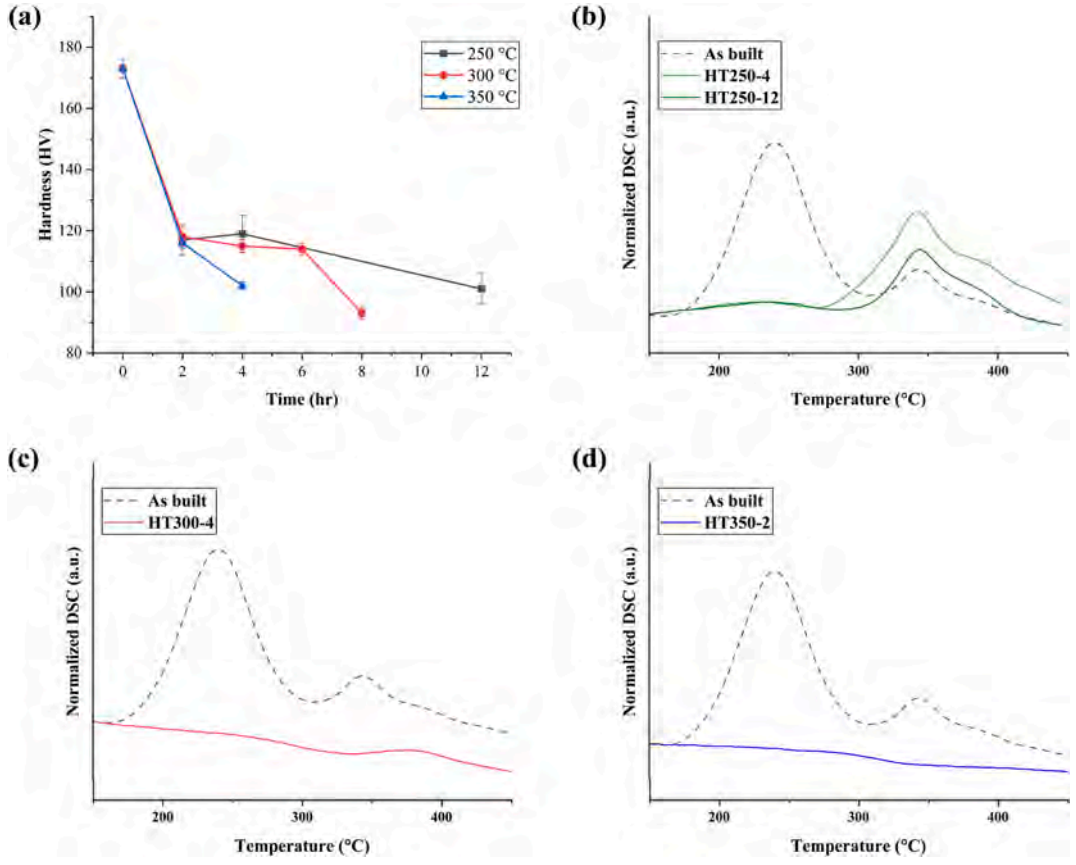

Fig. 6. (a) Evolution of Vickers microhardness in the AlSi10Cu8Mg alloy during the high-temperature aging regime (250–350 °C), and (b–d) normalized DSC curves comparing the as-built condition with selected aging treatments at (b) 250 °C, (c) 300 °C, and (d) 350 °C. Hardness values represent the mean ± standard deviation of ten indentations per condition.

temperature (~240 °C), the hardness decreases sharply to 117 HV0.5 within only 2 h. Further aging at 300 and 350 °C leads to continued degradation, reaching a minimum of 93 HV0.5. This decline corresponds to the flattened DSC trace observed for the HT350 condition (Fig. 6d), confirming a fully over-aged, near-equilibrium microstructure in which the silicon network has fragmented and the precipitates have coarsened into incoherent, non-strengthening phases. In conclusion, the as-built hardness (173 HV0.5) and peak-aged hardness (191 HV0.5) exceed those reported for AlSi10Cu4Mg (155 HV in AB, 180 HV peak) and AlSi10Mg (120–130 HV in AB, 145 HV peak) [23,51,53], confirming the strengthening contribution of increased Cu content.

To gain further insight, the treatments at 250 °C (Fig. 6b) reveal a critical change in microstructural stability. For the 4 h sample (HT250-4), the first peak is absent, as expected, since the aging temperature exceeds the temperature range of the first transformation, but the second peak becomes substantially taller than in the as-built condition. This indicates that the short 4 h treatment generated a large population of metastable precipitates that serve as efficient heterogeneous nucleation sites for the equilibrium phase. During DSC heating, this results in an accelerated, highly energetic transformation, producing a pronounced heat-flow spike. In contrast, the 12 h sample (HT250-12) exhibits a reduced second peak. This suggests that extended exposure at 250 °C allows significant coarsening within the furnace, causing precipitates to grow, lose coherency, and release internal energy before the DSC test, thereby lowering the exothermic signal. Prior studies [24,51] have documented the crystallization of θ-Al_2Cu and Si during overaging in similar alloy compositions, confirming the formation of coarser and more stable precipitates in the aged condition.

The DSC curves for 300 and 350 °C (Fig. 6c and d) display a flattened baseline in the low-temperature region and a greatly diminished second peak. These trends confirm that the material has reached its equilibrium state during the HT process itself, leaving no residual supersaturation or metastable phases available for further transformation during DSC heating.

3.3. Microstructural evolution and phase analysis

As demonstrated by several previous studies in the literature on similar alloy systems, albeit with lower Cu contents, the addition of Cu to the base AlSi10Mg composition promotes both an increased solid solution strengthening and the formation of Cu-rich precipitates. These microstructural modifications generally result in a significant increase in strength and hardness, at the expense of ductility [21].

This trend has already been partially confirmed in the alloy system investigated in the present work, AlSi10Cu8Mg. In particular, the as-built condition exhibits a marked increase in hardness, reaching values approximately 33 % higher than those of the reference AlSi10Mg alloy. This observation is consistent with the combined contributions of Cu in solid solution and early-stage precipitation occurring during the PBF-LB/M process.

In this context, post-processing heat treatments enable a targeted modulation of the mechanical response through the evolution of Cu-rich precipitates. Based on the trends already highlighted, the discussion is therefore restricted to two representative heat treatment conditions, which effectively describe the dominant low- and high-temperature precipitation mechanisms governing the strength–ductility trade-off.

For the low-temperature regime, the HT160-24 condition was selected as it represents a kinetically efficient aging treatment, exhibiting a markedly faster precipitation kinetics compared to 140 °C, while remaining compatible with industrial time constraints. The choice of a 24 h duration is supported by DSC results indicating the completion of the precipitation process, and it additionally provides sufficient time to promote precipitate reorganization. Such microstructural evolution is expected to mitigate excessive strain localization and therefore contribute positively to ductility.

For the high-temperature regime, the HT250-4 condition was selected as it enables the full precipitation sequence and significant precipitate coarsening to occur within a limited processing time, which is particularly attractive from an industrial perspective. Despite the accelerated kinetics, this condition does not lead to a pronounced degradation of mechanical strength, as evidenced by hardness values comparable to those measured after shorter treatments (2 h), indicating that further coarsening does not result in a substantial loss of strengthening.

The SEM analysis reveals two clearly distinct microstructural states, reflecting the different precipitation regimes induced by the selected heat treatments and directly controlling the resulting mechanical behavior of the alloy. In the HT160-24 condition (Fig. 7), the characteristic cellular architecture of the as-built PBF-LB/M material is largely retained. The high-magnification SEM images reveal a continuous Al–Si–Cu-rich interdendritic network surrounding the α-Al cells. This preserved cellular structure indicates that aging at 160 °C promotes precipitation without causing significant coarsening or fragmentation of the solidification substructure. As a result, the continuous network and fine Cu-rich precipitates remain effective barriers to dislocation motion, contributing to the high hardness measured in this condition. However, the same continuous network may also provide preferential paths for crack propagation, explaining the limited ductility observed after HT160-24.

This microstructural stability accounts for the high hardness measured in this condition (Fig. 5a). The intact silicon skeleton provides strong resistance to dislocation motion, while fine intracrystalline precipitates, consistent with the complete consumption of the DSC first exothermic peak (Fig. 5c), further increase the resistance to dislocation motion. However, the same continuous network also offers an uninterrupted path for crack propagation. The average cell size of HT160-24, measured at approximately 0.8 μm, is consistent with literature values reported for AlSi10Mg-based alloys and AlSi10Mg + Cu compositions [46]. This confirms that sub-micron cellular networks produced by PBF-LB/M remain highly stable and show limited coarsening under low temperature aging.

In contrast, the HT250-4 condition (Fig. 8) exhibits clear microstructural decomposition. The continuous cellular Al–Si–Cu-rich network observed after low-temperature aging is partially broken down and transformed into fragmented and spheroidized particles located mainly along the former cell boundaries. These fragments correspond to the thermally decomposed remnants of the original interdendritic/eutectic network. In addition, bright particles are visible within the Al matrix and are attributed mainly to coarsened Cu-rich precipitates, likely Al_2Cu-rich phases, with the possible contribution of Q-phase particles [44]. Within the examined regions, these fragments and precipitates appear relatively homogeneously distributed throughout the matrix; however, local variations are still observed near melt pool boundaries, where solute segregation is more pronounced due to the repeated melting and solidification cycles during PBF-LB/M. This coarsening and loss of cellular connectivity reduce the effectiveness of the network as a barrier to dislocation motion, explaining the decrease in hardness and strength to 119 HV0.5 (Fig. 6a). At the same time, the more discontinuous and relaxed microstructure allows greater plastic deformation, leading to the improved ductility observed in the HT250-4 condition.

Similar microstructural evolution has been reported for thermally treated PBF-LB/M AlSi10Mg alloys. Batalha et al. observed that increasing aging temperature disrupted the eutectic Si-rich cellular network and promoted coarsening of Si particles, accompanied by a reduction in strength [32]. Comparable decomposition of the Si-rich cellular structure has also been reported under local laser heat treatment. Kramer et al. observed progressive fragmentation of the Si-rich cellular network and agglomeration of Si particles with increasing thermal exposure, resulting in reduced hardness [34].

XRD analyses were performed to identify the phase constituents and assess microstructural evolution across the different conditions.

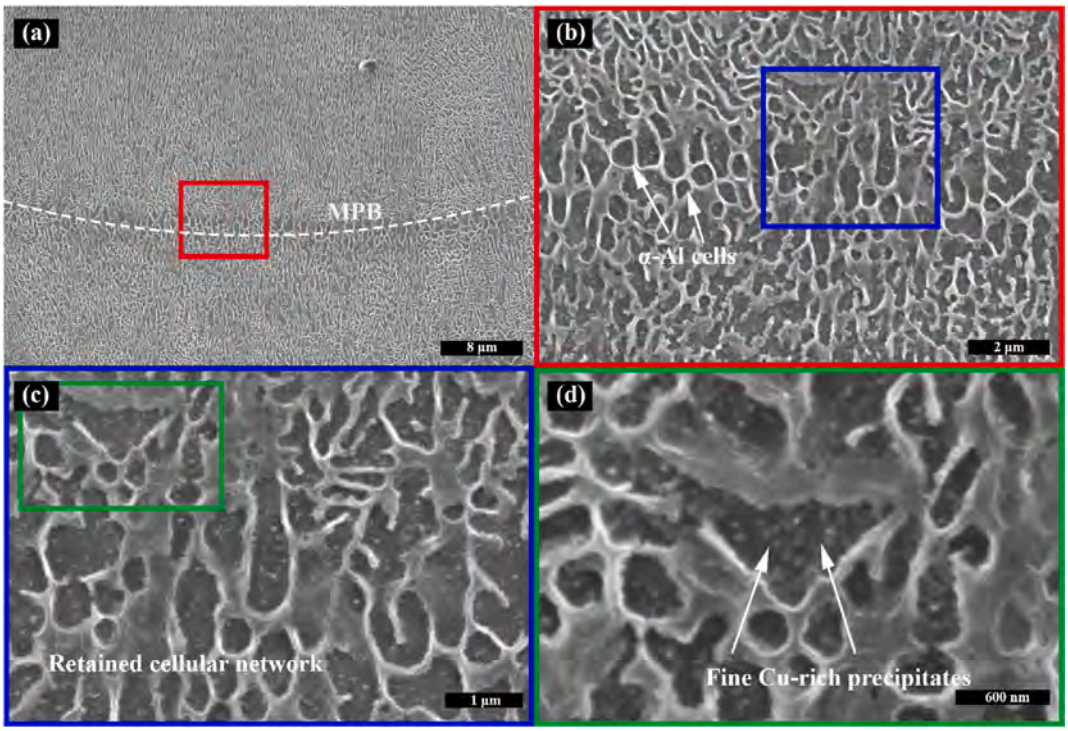

Fig. 7. SEM micrographs of the HT160-24 condition showing the retained PBF-LB/M cellular microstructure after low-temperature aging: (a) overview near the melt pool boundary, (b,c) higher-magnification views of α-Al cells surrounded by a continuous Al–Si–Cu-rich network, and (d) fine Cu-rich precipitates within the preserved cellular structure.

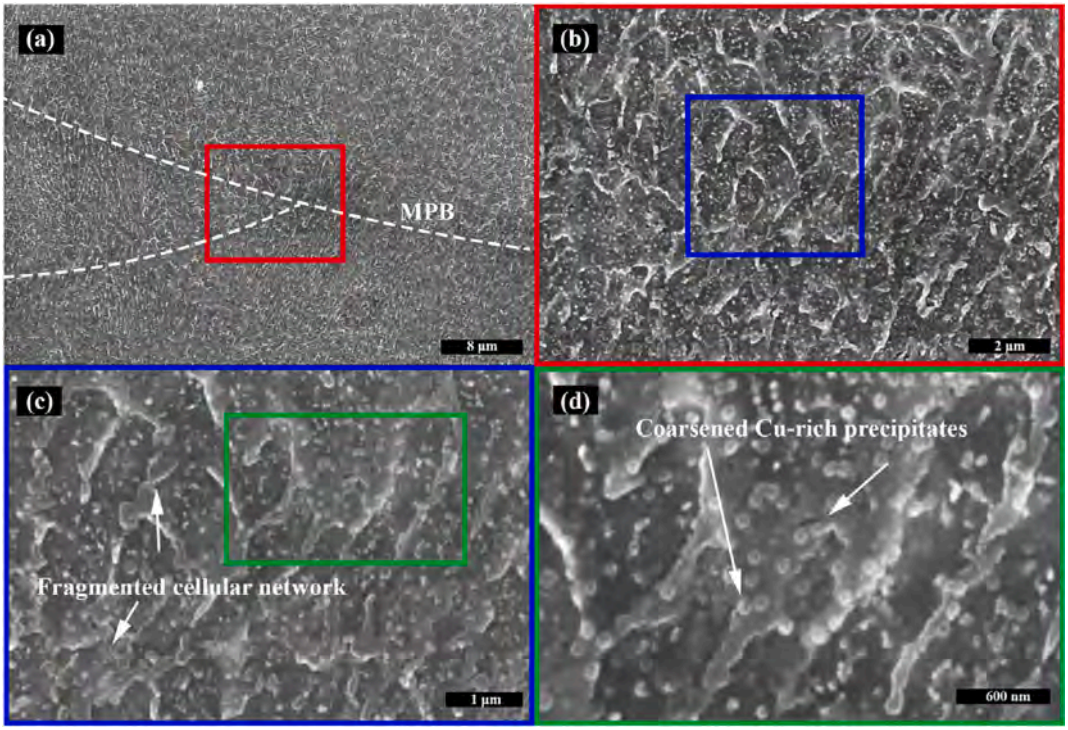

Figure 8. SEM micrographs of the HT250-4 condition showing microstructural decomposition after high-temperature aging: (a) overview near the melt pool boundary, (b,c) fragmented cellular network and former cell boundaries, and (d) spheroidized/coarsened Cu-rich precipitates distributed within the Al matrix.

Comparative analysis of the diffraction patterns reveals that three main phases, α-Al, Si, and θ-Al_2Cu, are present in all investigated states, as-built, HT160-24, and HT250-4 (Fig. 9). To further evaluate the evolution of solute supersaturation during thermal treatment, the lattice parameter of the α-Al phase was determined from the diffraction data, yielding values of 4.0408 Å for the as-built condition, 4.0531 Å for HT160-24, and 4.0522 Å for HT250-4. The lower value measured in the as-built condition indicates a shift in the α-Al diffraction peaks relative

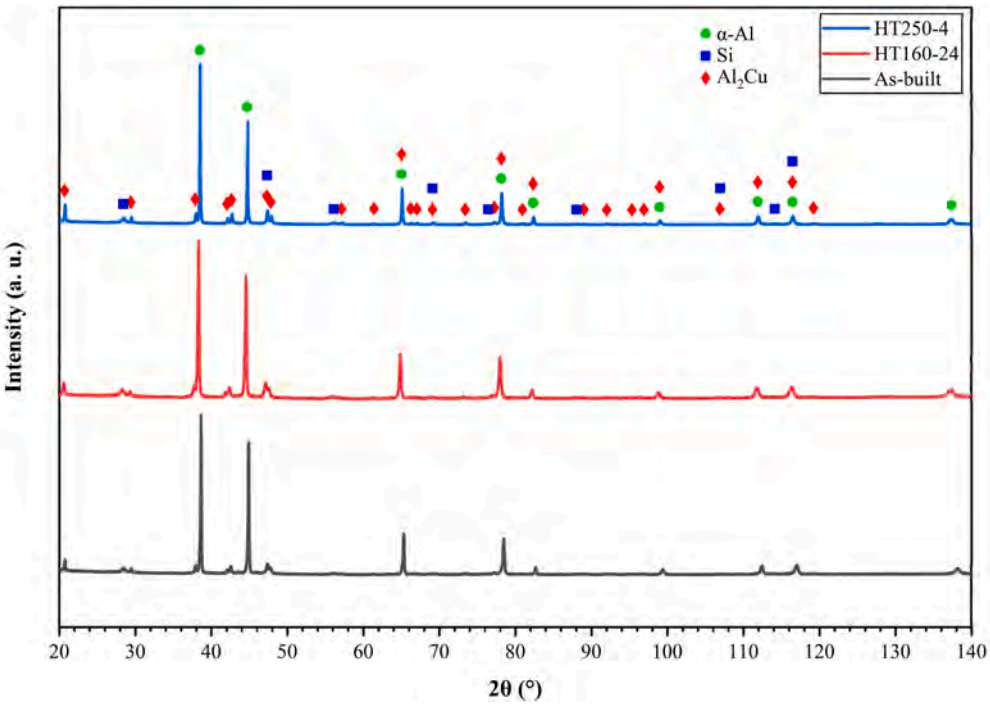

Fig. 9. XRD patterns of the PBF-LB/M AlSi10Cu8Mg alloy in the (a) as-built, (b) HT160-24, and (c) HT250-4 conditions.

to the heat-treated conditions. Retention of alloying elements, particularly Si and Cu, within the α-Al matrix may contribute to this relatively low value. However, the measured peak positions may also be influenced by residual elastic strain, microstrain, crystallographic texture, and experimental uncertainty. In addition, the simultaneous detection of Si and θ-Al_2Cu confirms that the nominal Si and Cu contents were not retained entirely within the α-Al solid solution.

After HT160-24 and HT250-4, the α-Al diffraction peaks shifted slightly toward lower 2θ values, corresponding to an increase in the apparent lattice parameter. This change is qualitatively consistent with solute redistribution and precipitation during aging, which may reduce the amount of lattice-contracting solute retained within the α-Al matrix. Residual-stress relaxation and changes in microstrain may also contribute to the observed peak shifts.

The principal XRD-detectable phases remained α-Al, Si, and θ-Al_2Cu after both heat treatments. No additional crystalline phase was detected after HT160-24, suggesting that the associated precipitation and solute-redistribution reactions either involved the phases already present or occurred at a size or volume fraction below the XRD detection limit. After HT250-4, the Si and θ-Al_2Cu reflections became more pronounced. Together with the SEM observations, this behavior is consistent with the redistribution and coarsening of Si- and Cu-rich constituents during high-temperature aging. Nevertheless, diffraction-peak intensity may also be affected by crystallographic texture, crystallite size, and phase fraction.

3.4. Near-surface residual-stress evaluation

To compare the near-surface thermal-relaxation response of the investigated conditions, X-ray residual-stress measurements were performed on the as-built, HT160-24, and HT250-4 cubic specimens (Fig. 10). The as-built condition exhibited a mean near-surface tensile residual stress of 127.5 ± 31 MPa. After HT160-24, this value decreased to 89 ± 7 MPa, corresponding to an approximate reduction of 30 %. A further decrease to 64 ± 9 MPa was measured after HT250-4, corresponding to an approximate reduction of 50 % relative to the as-built cubic specimens. These results demonstrate that direct aging progressively reduced the local near-surface tensile stress measured under the present experimental conditions.

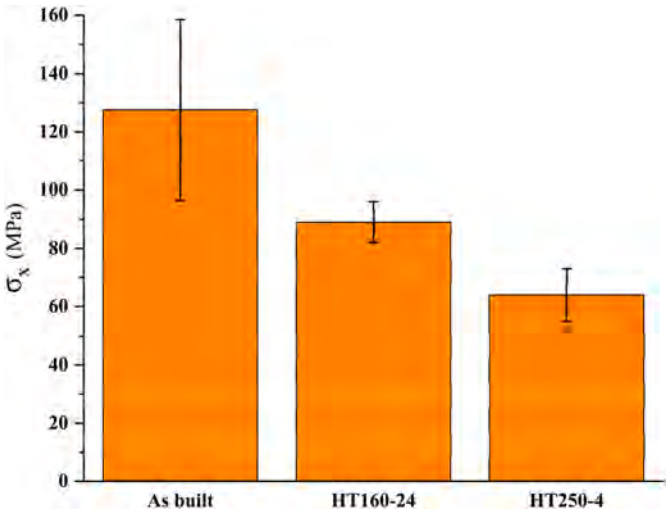

Figure 10. Surface residual stresses measured by X-ray diffraction for the as-built, HT160-24, and HT250-4 conditions. Error bars represent the standard deviation of five measurements performed along the build direction.

The EBSD analysis further supports the residual stress evolution measured by XRD, while also capturing the distinct microstructural modifications induced by the two heat treatments (Fig. 11). In the orientation maps, different colors correspond to different crystallographic orientations. High-angle grain boundaries (HAGBs, $> 15°$) are highlighted in black, while low-angle grain boundaries (LAGBs, $< 15°$) are shown in red; grains are defined as regions enclosed by HAGBs. In the as-built condition, the high density of LAGBs reflects a significant amount of stored strain, associated with the high dislocation density generated during rapid solidification and cooling. This is consistent with the elevated residual stresses measured by XRD.

Upon heat treatment, a progressive reduction in LAGB density is observed, indicating dislocation annihilation and rearrangement

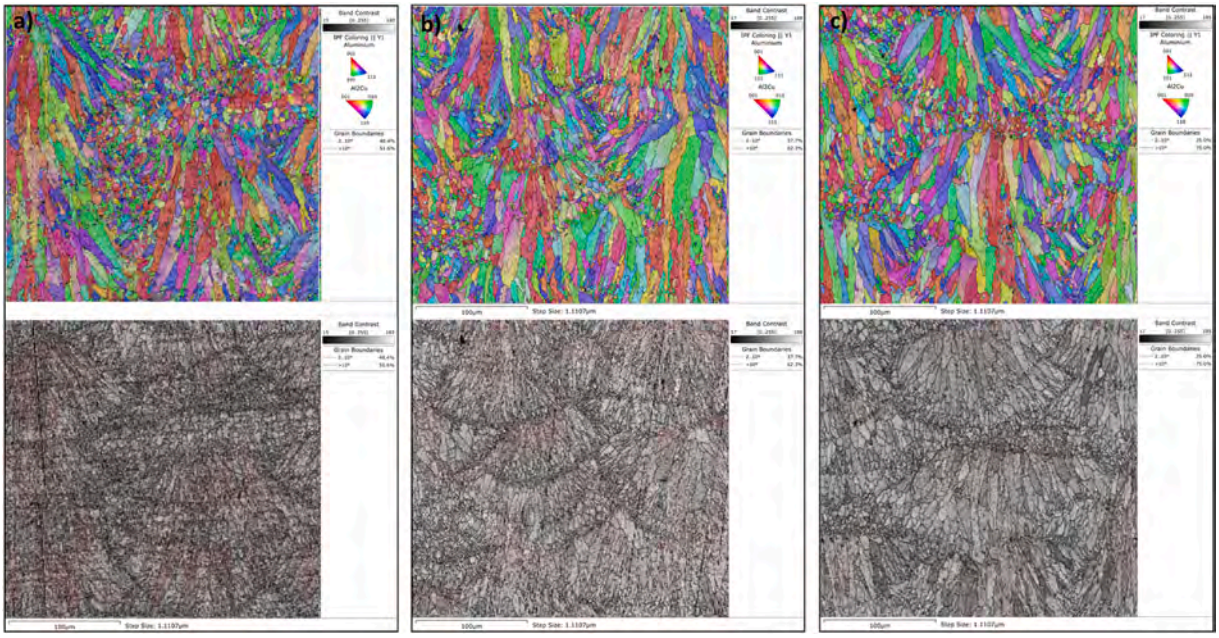

Figure 11. EBSD orientation maps (top) and corresponding grain boundary maps (bottom) of the AlSi10Cu8Mg alloy (a) as-built, (b) HT160-24, and (c) HT250-4 conditions.

through recovery mechanisms, in agreement with literature reports [54, 55]. In the HT160-24 condition, this reduction is moderate, suggesting partial stress relaxation. This occurs alongside significant precipitation, as evidenced by DSC/XRD, while the Al–Si–Cu cellular network remains largely intact, preserving the as-built microstructural framework. A more pronounced decrease in LAGBs is observed in the HT250-4 condition, consistent with the lower residual stress measured by XRD. This reflects more advanced recovery and microstructural evolution. At this temperature, SEM and XRD results indicate precipitate coarsening and growth of existing phases, accompanied by a partial degradation of the fine cellular network.

3.5. Mechanical properties

The engineering stress–strain curves for the PBF-LB/M AlSi10Cu8Mg alloy in the as-built, HT160-24 and HT250-4 states at room temperature are shown in Fig. 12a, while the corresponding elevated-temperature curves at 200 °C for the as-built and two heat-treated conditions are presented in Fig. 12b and the quantitative values are summarized in Table 3. These results reveal a pronounced dependence on thermal history and illustrate a clear strength–ductility trade-off.

Table 3
Mechanical properties of the AlSi10Cu8Mg alloy in the as-built and heat-treated conditions at room temperature and 200 °C. Values are reported as mean ± standard deviation from five specimens per condition.

Specimen	Yield strength (MPa)	Ultimate tensile strength (MPa)	Post-yield strengthening (MPa)	Elongation (%)
Room temperature				
As-built	372 ± 2.1	400 ± 19.8	28	0.93 ± 0.1
HT160-24	375 ± 4.7	388 ± 32.5	13	0.76 ± 0.1
HT250-4	268 ± 5.1	350 ± 28.6	82	1.40 ± 0.2
Elevated temperature (200 °C)				
As-built	286 ± 3.8	367 ± 20.18	81	2.28 ± 0.3
HT160-24	277 ± 10.2	307 ± 17.5	30	0.95 ± 0.2
HT250-4	215 ± 7.3	302 ± 22.4	87	2.6 ± 0.2

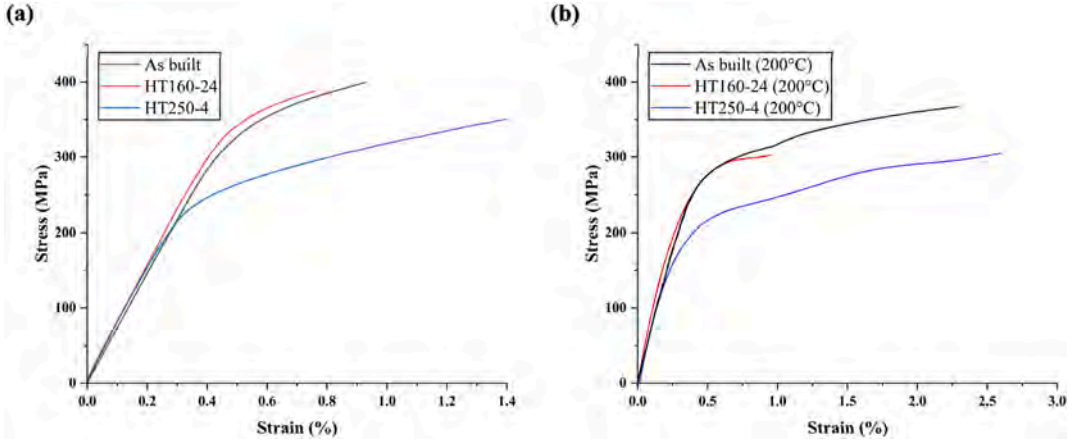

Figure 12. Representative engineering stress–strain curves of the PBF-LB/M AlSi10Cu8Mg alloy under different aging treatments. (a) Room-temperature tensile response, and (b) Elevated-temperature tensile behavior at 200 °C.

At room temperature, the as-built alloy exhibits yield stress of 372 and ultimate stress of 400 MPa but fractures at only 0.93 % strain, consistent with its fine cellular microstructure, residual stresses, and typical PBF-LB/M defects that restrict ductility. HT160-24 achieves a slightly higher yield strength, while exhibiting an ultimate tensile strength comparable to the other conditions. However, it displays the lowest elongation (0.76 %), consistent with the presence of a dense distribution of fine, coherent precipitates that effectively impede dislocation motion. In contrast, HT250-4 represents an over-aged condition. At room temperature, the yield strength decreases to 268 MPa, corresponding to a reduction of about 30 % compared to both the as-built state and HT160-24. The ultimate tensile strength drops to 350 MPa, approximately 10 % lower than as-built and HT160-24 conditions. Conversely, ductility increases to 1.40 %, representing an improvement of about 50 % with respect to the as-built state and approximately 85 % compared to HT160-24. This behavior is attributed to precipitate coarsening, increased inter-particle spacing, and partial relaxation of internal stresses, all of which enhance the alloy capacity for plastic deformation.

To further assess the post-yield deformation capacity, the difference between ultimate tensile strength and yield strength was considered as a simple indicator of post-yield strengthening. At room temperature, the as-built and HT160-24 conditions show very limited post-yield strengthening, with UTS–YS values of only 28 MPa and 13 MPa, respectively. This agrees with their low elongation values of 0.93 % and 0.76 %, indicating rapid strain localization after yielding. In contrast, HT250-4 exhibits a much larger UTS–YS difference of 82 MPa, together with improved elongation of 1.40 %, confirming its greater ability to accommodate plastic deformation. At 200 °C, the same trend is observed: HT250-4 shows the largest UTS–YS difference of 87 MPa, compared with 81 MPa for the as-built condition and 30 MPa for HT160-24. This behavior is consistent with the fragmented cellular network, coarsened Cu-rich/Al_2Cu-rich particles, and reduced residual stress measured after high-temperature aging.

When tensile tests are conducted at 200 °C, the material exhibits a general reduction in flow stress accompanied by a marked increase in ductility across all conditions, consistent with thermally activated softening. At this temperature, the as-built condition shows a decrease in yield strength from 372 to 286 MPa (around 20 %) and in ultimate tensile strength from 400 to 367 MPa (less than 10 %), while elongation increases markedly from 0.93 to 2.28 % (+145 %). This indicates a substantially enhanced ductile response at elevated temperature, achieved without a severe loss of strength. For HT160-24, the yield strength and ultimate tensile strength drop by about 20 % in values, with only a limited increase in elongation (+25 %). This behavior is attributed to in-situ over-aging above the original aging temperature, which accelerates precipitate coarsening and promotes strain localization. In contrast, HT250-4 tested at a temperature below its original aging temperature, demonstrates superior thermal stability: although the yield strength decreases to 215 MPa (−20 %), the elongation increases significantly to 2.6 % (+85 %). The relatively stable precipitate distribution, together with thermally activated deformation mechanisms such as dislocation climb and cross-slip, enables substantial plastic deformation without premature brittle fracture.

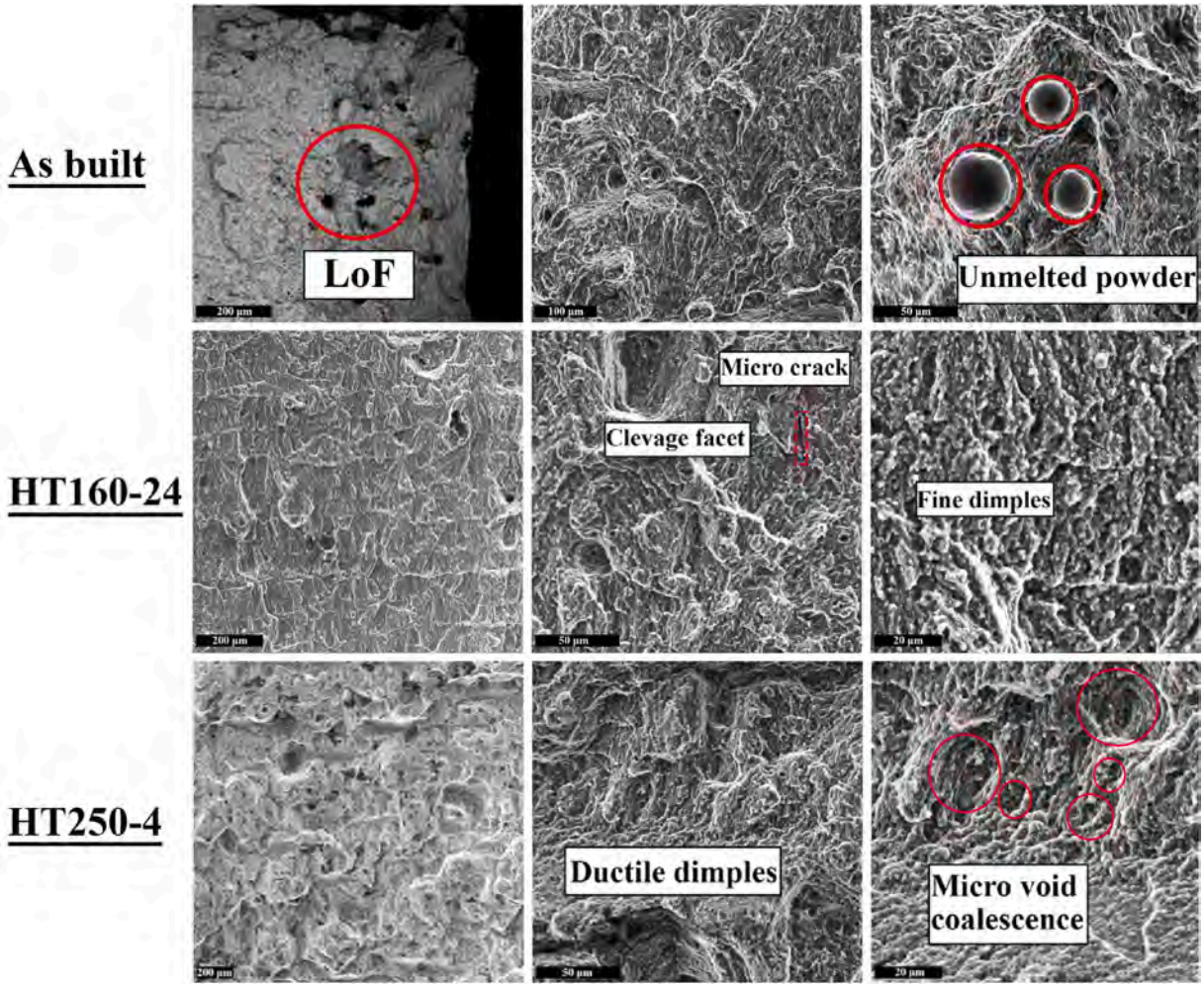

Figure 13. SEM fractographs of the tensile fracture surfaces: (Top Row) As-built condition; (Middle Row) HT160-24 condition; (Bottom Row) HT250-4 condition.

The fracture surfaces of the tensile specimens were examined by SEM to elucidate the failure mechanisms associated with the different thermal histories (Fig. 13). A clear correlation was observed between the fracture morphology and the mechanical behavior recorded in the stress–strain curves. In the as-built condition (Fig. 13 top row), low-magnification micrographs show a relatively irregular fracture surface containing processing defects such as lack-of-fusion regions and gas pores. At higher magnification, partially melted or unmelted powder particles can be identified on and near the fracture surface. These defects act as local stress concentrators and preferential crack-initiation sites, facilitating early crack propagation and thereby limiting the macroscopic ductility of the as-built material.

Following heat treatment at 160 °C for 24 h (Fig. 13 middle row), the fracture morphology becomes more tortuous and locally flatter, with regions that exhibit faceted features and vein-like patterns. Together with areas covered by fine, closely spaced dimples, this indicates a mixed quasi-cleavage/ductile fracture mode. This behavior is consistent with the material being near peak strength: precipitation hardening increases the resistance to dislocation motion, restricting plastic flow and reducing the strain-to-failure (0.76 %), while still allowing limited micro-void nucleation and coalescence. In contrast, the specimens heat treated at 250 °C for 4 h (Fig. 13 bottom row) display a fracture surface characteristic of ductile rupture. High-magnification micrographs reveal a dense population of large, deep, equiaxed dimples formed by extensive micro-void growth and coalescence. This pronounced dimpled morphology reflects significant thermal softening and over-aging of the microstructure, where precipitate coarsening and stress relief reduce the resistance to dislocation motion. As a result, the material accommodates greater plastic deformation prior to failure, in agreement with the tensile data, which show the highest elongation to failure (1.4 %) accompanied by a reduction in ultimate tensile strength.

Overall, the fractography confirms the strong link between processing condition, microstructural evolution and mechanical response. Aging at 160 °C for 24 h produces a strengthened but less ductile material with a mixed quasi-cleavage/ductile fracture mode, while the higher-temperature treatment at 250 °C for 4 h results in a much more ductile fracture surface dominated by deep dimples, characteristic of an over-aged and stress-relieved microstructure with reduced strength but enhanced ductility.

3.6. Microstructure–property correlation

The results obtained in this study show that the mechanical response of PBF-LB/M AlSi10Cu8Mg is governed by the combined effects of the process-induced cellular architecture, phase constitution, precipitation-related reactions, residual stress state, and thermal stability of the Al–Si–Cu-rich network. In the as-built condition, rapid solidification during PBF-LB/M produces a fine cellular/dendritic microstructure with Si and Cu enrichment along the interdendritic regions. XRD analysis confirms that the main detectable crystalline phases are α-Al, Si, and θ-Al_2Cu, indicating that part of the Cu is already present as crystalline Al_2Cu-rich constituents after solidification. This phase constitution, together with the fine cellular network and residual solute supersaturation, contributes to the high strength of the as-built alloy. EBSD analysis further reveals a high density of low-angle grain boundaries, reflecting significant stored strain and a high dislocation density induced by rapid solidification, in agreement with the elevated residual stresses measured by XRD. However, the same continuous cellular network, residual tensile stresses, and local processing defects restrict plastic deformation and promote early crack initiation, resulting in limited elongation.

The low-temperature aging regime, particularly HT160-24, preserves the original cellular architecture while promoting precipitation-related strengthening, as supported by the DSC response and hardness evolution. XRD does not reveal major changes in the detectable phase constitution after HT160-24 compared with the as-built condition, suggesting that the strengthening effect mainly arises from fine-scale precipitation and solute redistribution below the detection limit of conventional XRD. EBSD shows a moderate reduction in LAGB density, indicating partial dislocation recovery and stress relaxation, while the overall microstructural framework remains largely unchanged. This condition maintains high yield strength because the retained cellular Al–Si–Cu-rich network and fine strengthening features effectively hinder dislocation motion. However, the continuous network also limits strain accommodation and provides preferential paths for crack propagation. The residual stress results help explain the mechanical response: in HT160-24, although residual stresses are partially relieved (from 127.5 ± 31 MPa to 89 ± 7 MPa), the retained continuous network and fine precipitates still constrain plastic deformation, resulting in limited elongation.

In contrast, the HT250-4 condition produces a more relaxed and partially over-aged microstructure, characterized by fragmentation of the cellular network and spheroidization/coarsening of Cu-rich/Al_2Cu-rich particles. The XRD patterns show more pronounced Si and θ-Al_2Cu reflections, consistent with coarsening and/or improved crystallinity of Si- and Cu-rich phases during high-temperature aging. EBSD analysis highlights a more pronounced reduction in LAGB density, indicating enhanced recovery and a lower stored strain state, in agreement with the further decrease in residual stress (down to 64 ± 9 MPa). This microstructural evolution reduces the effectiveness of the cellular network and precipitates as barriers to dislocation motion, leading to lower hardness and strength. At the same time, the discontinuous network, increased inter-particle spacing, and stronger residual stress relaxation allow more homogeneous plastic deformation before fracture. As a result, HT250-4 exhibits improved elongation and a more ductile fracture morphology. In this condition, the combination of reduced residual stress, network fragmentation, and precipitate coarsening enhances strain accommodation and damage tolerance, explaining the higher elongation observed at both room temperature and 200 °C.

The elevated-temperature tensile results further support this interpretation. At 200 °C, the HT160-24 condition is tested above its original aging temperature, which may promote additional in-situ over-aging and reduce mechanical stability during deformation. Conversely, HT250-4 is aged above the testing temperature and therefore exhibits a more stable monotonic response, showing the highest elongation among the investigated conditions at 200 °C. However, the 200 °C tensile tests should be interpreted as a short-term monotonic assessment of elevated-temperature mechanical response.

Overall, these results demonstrate that the strength–ductility balance in PBF-LB/M AlSi10Cu8Mg is controlled not only by precipitation-related strengthening, but also by the stability or fragmentation of the cellular Al–Si–Cu-rich network and the extent of residual stress relaxation. Preserving the cellular network maximizes hardness and strength but limits plasticity, whereas controlled fragmentation and coarsening reduce strength while improving ductility and damage tolerance.

4. Conclusions

This study investigated the direct-aging response of a pre-alloyed AlSi10Cu8Mg alloy fabricated by PBF-LB/M, with particular attention to the relationships among heat-treatment temperature, hardness evolution, cellular-network stability, residual stress, and mechanical performance. The principal conclusions are as follows:

- The optimized PBF-LB/M parameters of 250 W laser power and 1250 mm/s scan speed produced specimens with a relative density of approximately 99.9 %. The as-built alloy exhibited a fine cellular/dendritic microstructure enriched in Si and Cu along the interdendritic regions. This condition showed a hardness of 173 HV0.5, a yield strength of 372 MPa, an ultimate tensile strength of 400 MPa, and an elongation of 0.93 %.

- Low-temperature direct aging produced a clear age-hardening response. The maximum hardness of 191 HV0.5 was obtained after aging at 160 °C for 10 h. After aging at 160 °C for 24 h, the cellular Al–Si–Cu-rich network remained largely continuous, and the alloy retained a yield strength of 375 MPa and an ultimate tensile strength of 388 MPa, albeit at the expense of a slight reduction in elongation at fracture.
- Aging at 250 °C for 4 h promoted fragmentation of the cellular network and coarsening and redistribution of Si- and Cu-rich particles. The hardness decreased to approximately 119 HV0.5, while the yield strength and ultimate tensile strength decreased to 268 and 350 MPa, respectively. In contrast, elongation increased above 50 % compared to the as-built condition and by 84 % compared to after HT160-24.
- Direct aging reduced the measured near-surface residual stress from 127.5 ± 31 MPa in the as-built condition to 89 ± 7 MPa after HT160-24 and 64 ± 9 MPa after HT250-4. These results correspond to reductions of approximately 30 and 50 %, respectively.
- At 200 °C, the as-built alloy exhibited a yield strength of 286 MPa, an ultimate tensile strength of 367 MPa, and an elongation of 2.28 %. HT160-24 showed lower elevated-temperature stability. HT250-4 provided the greatest elevated-temperature elongation, while maintaining a yield strength of 215 MPa and an ultimate tensile strength of 302 MPa.

Overall, the results demonstrate that the mechanical response of PBF-LB/M AlSi10Cu8Mg is controlled by both precipitation-related processes and the thermal stability of the cellular Al–Si–Cu-rich network. Low-temperature aging maximized hardness and yield strength, whereas HT250-4 provided the most balanced combination of strength, ductility, short-term elevated-temperature performance, and processing duration among the investigated conditions.

Declaration of competing interest

The authors declare that they have no known competing financial interests or personal relationships that could have appeared to influence the work reported in this paper.

Acknowledgments

The authors gratefully acknowledge Hamidreza Ghayour and Francesco Pisapia for their valuable contributions and support throughout this research.

References

[1] Yadegari MJ, Zeinoddini M, Ezzati M, Kashani-Bozorg SF, Miresmaeili R, Ghafoori E. On collapse of 3D printed thin-walled PBF-LB/M 316L stainless steels under inelastic stress cycling. Thin-Walled Struct 2025;215:113413. https://doi.org/10.1016/j.tws.2025.113413.

[2] Berrocal L, Fernández R, González S, Periñán A, Tudela S, Vilanova J, Rubio L, Martín Márquez JM, Guerrero J, Lasagni F. Topology optimization and additive manufacturing for aerospace components. Progr Addit Manuf 2019;4:83–95. https://doi.org/10.1007/s40964-018-0061-3.

[3] Ford S, Despeisse M. Additive manufacturing and sustainability: an exploratory study of the advantages and challenges. J Clean Prod 2016;137:1573–87. https://doi.org/10.1016/j.jclepro.2016.04.150.

[4] Xi L, Lu Q, Gu D, Cao S, Zhang H, Kaban I, Sarac B, Prashanth KG, Eckert J. Circumventing solidification cracking susceptibility in Al–Cu alloys prepared by laser powder bed fusion, 3D Print. Addit Manuf 2024;11:e731–42. https://doi.org/10.1089/3dp.2022.0207.

[5] Rometsch PA, Zhu Y, Wu X, Huang A. Review of high-strength aluminium alloys for additive manufacturing by laser powder bed fusion. Mater Des 2022;219:110779. https://doi.org/10.1016/j.matdes.2022.110779.

[6] Kotadia HR, Gibbons G, Das A, Howes PD. A review of laser powder bed fusion additive manufacturing of aluminium alloys: microstructure and properties. Addit Manuf 2021;46:102155. https://doi.org/10.1016/j.addma.2021.102155.

[7] Marola S, Fiore G, Battezzati L. Effect of modifiers on the microstructure of rapidly solidified AlSi10Mg alloy. Metall Mater Trans 2023;54:624–33. https://doi.org/10.1007/s11661-022-06907-8.

[8] Hyer H, Zhou L, Mehta A, Park S, Huynh T, Song S, Bai Y, Cho K, McWilliams B, Sohn Y. Composition-dependent solidification cracking of aluminum-silicon alloys during laser powder bed fusion. Acta Mater 2021;208:116698. https://doi.org/10.1016/j.actamat.2021.116698.

[9] Yadegari MJ, Martucci A, Biamino S, Ugues D, Montanaro L, Fino P, Lombardi M. Aluminum laser additive manufacturing: a review on challenges and opportunities through the lens of sustainability. Appl Sci 2025;15:2221. https://doi.org/10.3390/app15042221.

[10] Wang JG, Wang ZT. Advance on wrought aluminium alloys used for aeronautic and astronautic industry (1), Light Alloy Fabrication Technology, vol. 41; 2013. p. 1–6.

[11] Pourkhorshid E, Rometsch P, Chen X-G. Laser-based additive manufacturing processability and mechanical properties of Al-Cu 224 alloys with TiB grain refiner additions. Materials 2025;18:516. https://doi.org/10.3390/ma18030516.

[12] Shi Z, Yan P, Yan B. Solidification mechanism of microstructure of Al-Si-Cu-Ni alloy manufactured by laser powder bed fusion and mechanical properties effect. Metals 2024;14:586. https://doi.org/10.3390/met14050586.

[13] Wang Y, Lin X, Zhao Y, Zhang T, Fu J, Zheng N, Wang Z, Huang W. Cracking mechanism and its susceptibility to scanning speed during laser power bed fusion processed high-strength 2024Al alloy. Mater Charact 2022;194:112344. https://doi.org/10.1016/j.matchar.2022.112344.

[14] Nie X, Chen Z, Qi Y, Zhang H, Zhu H. Spreading behavior and hot cracking mechanism of single tracks in high strength Al–Cu–Mg–Mn alloy fabricated by laser powder bed fusion. Acta Metall Sin 2023;36:1454–64. https://doi.org/10.1007/s40195-023-01553-4.

[15] Garmendia X, Chalker S, Bilton M, Sutcliffe CJ, Chalker PR. Microstructure and mechanical properties of Cu-modified AlSi10Mg fabricated by laser-powder bed fusion. Materialia 2020;9:100590. https://doi.org/10.1016/j.mtla.2020.100590.

[16] Hu L, Li Y, Luo G, Shi Q, Wang Y, Ma S, Cui Y, Wang H, Chen Z. Understanding cellular structure formation in rapidly solidified Al–Ni alloys by constructing solidification microstructure selection maps. Addit Manuf 2023;73:103671. https://doi.org/10.1016/j.addma.2023.103671.

[17] Ahuja B, Karg M, Nagulin KYu, Schmidt M. Fabrication and characterization of high strength Al-Cu alloys processed using laser beam melting in metal powder bed. Phys Procedia 2014;56:135–46. https://doi.org/10.1016/j.phpro.2014.08.156.

[18] Aversa A, Bosio F, Marola S, Lorusso M, Manfredi D, Battezzati L, Fino P, Lombardi M. Laser single scan tracks of new aluminium alloys compositions. In: Euro PM2018 proceedings: AM special materials. European Powder Metallurgy Association; 2018. p. 15–20.

[19] Bosio F, Aversa A, Lorusso M, Marola S, Gianoglio D, Battezzati L, Fino P, Manfredi D, Lombardi M. A time-saving and cost-effective method to process alloys by Laser Powder Bed Fusion. Mater Des 2019;181:107949. https://doi.org/10.1016/j.matdes.2019.107949.

[20] Marola S, Gianoglio D, Bosio F, Aversa A, Lorusso M, Manfredi D, Lombardi M, Battezzati L. Alloying AlSi10Mg and Cu powders in laser single scan tracks, melt spinning, and laser powder bed fusion. J Alloys Compd 2020;821:153538. https://doi.org/10.1016/j.jallcom.2019.153538.

[21] Bosio F, Fino P, Manfredi D, Lombardi M. Strengthening strategies for an Al alloy processed by in-situ alloying during laser powder bed fusion. Mater Des 2021;212:110247. https://doi.org/10.1016/j.matdes.2021.110247.

[22] Martucci A, Gobber F, Aversa A, Manfredi D, Fino P, Lombardi M. Improvement in the PBF-LB/M processing of the Al-Si-Cu-Mg composition through the use of pre-alloyed powder. Mater Res Express 2023;10:046508. https://doi.org/10.1088/2053-1591/acc82f.

[23] Martin A, San Sebastian M, Gil E, Wang CY, Milenkovic S, Pérez-Prado MT, Cepeda-Jiménez CM. Effect of the heat treatment on the microstructure and hardness evolution of a AlSi10MgCu alloy designed for laser powder bed fusion. Mater Sci Eng, A 2021;819:141487. https://doi.org/10.1016/j.msea.2021.141487.

[24] Martucci A, Aversa A, Bondioli F, Fino P, Lombardi M. Synergic strategies to improve the PBF-LB\M processability of a cracking-sensitive alloy. Mater Des 2022;224:111396. https://doi.org/10.1016/j.matdes.2022.111396.

[25] Rojas-Arias N, Coury FG, Vanmeensel K, Amancio-Filho ST, Gargarella P. Heat treating additive-manufactured alloys: a comprehensive review. J Alloys Compd 2024;1005:176035. https://doi.org/10.1016/j.jallcom.2024.176035.

[26] Laleh M, Sadeghi E, Revilla RI, Chao Q, Haghdadi N, Hughes AE, Xu W, De Graeve I, Qian M, Gibson I, Tan MY. Heat treatment for metal additive manufacturing. Prog Mater Sci 2023;133:101051. https://doi.org/10.1016/j.pmatsci.2022.101051.

[27] Fiocchi J, Tuissi A, Biffi CA. Heat treatment of aluminium alloys produced by laser powder bed fusion: a review. Mater Des 2021;204:109651. https://doi.org/10.1016/j.matdes.2021.109651.

[28] Toschi S. Optimization of A354 Al-Si-Cu-Mg alloy heat treatment: effect on microstructure, hardness, and tensile properties of peak aged and overaged alloy. Metals 2018;8:961. https://doi.org/10.3390/met8110961.

[29] Li X, Wang J, Yang X, Xue C, Wang S, Li Q, Miao Y, Meng Y, Kong D, Lang Y. Effect of solid solution treatment on the kinetics of hydrogen porosity evolution and mechanical properties in Al–Cu–Li alloys. Vacuum 2024;224:113157. https://doi.org/10.1016/j.vacuum.2024.113157.

[30] Megahed S, Bühring J, Duffe T, Bach A, Schröder K-U, Schleifenbaum JH. Effect of heat treatment on ductility and precipitation size of additively manufactured AlSi10Mg. Metals 2022;12:1311. https://doi.org/10.3390/met12081311.

[31] Maeshima T, Oh-ishi K, Kadoura H. Microstructural evolution and hardening phenomenon caused by aging of AlSi10Mg alloy by laser powder bed fusion. Heliyon 2024;10:e28006. https://doi.org/10.1016/J.HELIYON.2024.E28006.

[32] Batalha RL, Ferreira CM, Silva AC, Reis L, Cláudio R, Carmezim MJ, Ramasamy P, Godefroid LB, de Araújo SC, de Faria GL, Morais PJ. Direct aging of AlSi10Mg alloy

produced by powder bed fusion – laser beam: eliminating the need for solution heat treatment. J Mater Res Technol 2026;42:3057–71. https://doi.org/10.1016/J.JMRT.2026.03.256.
[33] Sathishkumar A, Soundararajan R, Sivasankaran S, Ramesh A. Comparative evaluation of microstructure, mechanical properties, and strengthening mechanisms in cast and selective laser melted AlSi10Mg alloys with direct aging treatment. Trans Nonferrous Met Soc China 2026;36:677–93. https://doi.org/10.1016/S1003-6326(25)66990-1.
[34] Kramer S, Jarwitz M, Graf T, Schulze V, Zanger F. Tuning the microstructure and mechanical properties of AlSi10Mg powder bed fusion (PBF-LB) parts by local laser heat treatment. Progr Addit Manuf 2026. https://doi.org/10.1007/s40964-026-01729-1.
[35] ASTM International. Test method for apparent density of non-free-flowing metal powders using the Carney Funnel. 2018. https://doi.org/10.1520/B0417-18.
[36] ASTM International. Test method for tap density of metal powders and compounds. https://doi.org/10.1520/B0527-24; 2024.
[37] Sutton AT, Kriewall CS, Leu MC, Newkirk JW. Powder characterisation techniques and effects of powder characteristics on part properties in powder-bed fusion processes. Virtual Phys Prototyp 2017;12:3–29. https://doi.org/10.1080/17452759.2016.1250605.
[38] ASTM International. Test method for microindentation hardness of materials. https://doi.org/10.1520/E0384-22; 2022.
[39] ASTM International. Test methods for tension testing of metallic materials. 2022. https://doi.org/10.1520/E0008_E0008M-22.
[40] Trevisan F, Calignano F, Lorusso M, Pakkanen J, Aversa A, Ambrosio E, Lombardi M, Fino P, Manfredi D. On the selective laser melting (SLM) of the AlSi10Mg alloy: process, microstructure, and mechanical properties. Materials 2017;10:76. https://doi.org/10.3390/ma10010076.
[41] Hou J, Chen W, Chen Z, Zhang K, Huang A. Microstructure, tensile properties and mechanical anisotropy of selective laser melted 304L stainless steel. J Mater Sci Technol 2020;48:63–71. https://doi.org/10.1016/j.jmst.2020.01.011.
[42] ASTM International. Test methods for determining average grain size. https://doi.org/10.1520/E0112-24; 2024.
[43] Wang J, Zhu R, Liu Y, Zhang L. Understanding melt pool characteristics in laser powder bed fusion: an overview of single- and multi-track melt pools for process optimization. Adv Powder Mater 2023;2:100137. https://doi.org/10.1016/j.apmate.2023.100137.
[44] Vanzetti M, Pavel MJ, Williamson CJ, Padovano E, Pérez-Andrade LI, Weaver M, Brewer LN, Bondioli F, Fino P. Design and characterization of innovative gas-atomized Al-Si-Cu-Mg alloys for additive manufacturing. Metals 2023;13:1845. https://doi.org/10.3390/met13111845.
[45] Van Cauwenbergh P, Samaee V, Thijs L, Nejezchlebová J, Sedlák P, Iveković A, Schryvers D, Van Hooreweder B, Vanmeensel K. Unravelling the multi-scale structure–property relationship of laser powder bed fusion processed and heat-treated AlSi10Mg. Sci Rep 2021;11:6423. https://doi.org/10.1038/s41598-021-85047-2.
[46] Ding L, Jia Z, Nie J-F, Weng Y, Cao L, Chen H, Wu X, Liu Q. The structural and compositional evolution of precipitates in Al-Mg-Si-Cu alloy. Acta Mater 2018;145:437–50. https://doi.org/10.1016/j.actamat.2017.12.036.
[47] Bobel A, Kim Y, Casalena L, Maddalena R, Sachdev AK. Microstructure and mechanical properties of a hypereutectic Al–Si–Cu alloy manufactured by laser powder bed fusion. Mater Sci Eng, A 2024;901:146549. https://doi.org/10.1016/j.msea.2024.146549.
[48] Marola S, Manfredi D, Fiore G, Poletti MG, Lombardi M, Fino P, Battezzati L. A comparison of Selective Laser Melting with bulk rapid solidification of AlSi10Mg alloy. J Alloys Compd 2018;742:271–9. https://doi.org/10.1016/j.jallcom.2018.01.309.
[49] Fiocchi J, Biffi CA, Colombo C, Vergani LM, Tuissi A. Ad Hoc heat treatments for selective laser melted Alsi10mg alloy aimed at stress-relieving and enhancing mechanical performances. JOM 2020;72:1118–27. https://doi.org/10.1007/s11837-019-03973-z.
[50] Fiocchi J, Tuissi A, Bassani P, Biffi CA. Low temperature annealing dedicated to AlSi10Mg selective laser melting products. J Alloys Compd 2017;695:3402–9. https://doi.org/10.1016/j.jallcom.2016.12.019.
[51] Martucci A, Bassini E, Lombardi M. Effect of Cu content on the PBF-LB/M processing of the promising Al-Si-Cu-Mg composition. Metals 2023;13:1315. https://doi.org/10.3390/met13071315.
[52] Hutchinson CR. Modeling the kinetics of precipitation in aluminium alloys. In: Fundamentals of aluminium metallurgy. Elsevier; 2011. p. 422–67. https://doi.org/10.1533/9780857090256.2.422.
[53] Mertens AI, Delahaye J, Lecomte-Beckers J. Fusion-based additive manufacturing for processing aluminum alloys: state-of-the-art and challenges. Adv Eng Mater 2017;19. https://doi.org/10.1002/adem.201700003.
[54] Rollett A, Humphreys F, Rohrer GS, Hatherly M. Recrystallization and related annealing phenomena. In: Recrystallization and related annealing phenomena. second ed. 2004. p. 1–628. Second Edition.
[55] Takata N, Kodaira H, Sekizawa K, Suzuki A, Kobashi M. Change in microstructure of selectively laser melted AlSi10Mg alloy with heat treatments. Mater Sci Eng, A 2017;704:218–28. https://doi.org/10.1016/j.msea.2017.08.029.